Mechanically Compliant Thermal Interfaces Using Biporous Copper-Polydimethylsiloxane Interpenetrating Phase Composite

Cheng-Hui Lin, Anna Guell Izard, Lorenzo Valdevit, and Yoonjin Won*

Thermal interface materials are essential for thermal management in electronics packaging by providing a low resistance thermal pathway between heat sources and heat sinks. Nanostructured materials can be potential candidates for the next-generation interface materials by coupling their high thermal conductivity and mechanical compliance, suppressing failure even after large numbers of thermal cycles. This work investigates the thermal and mechanical characteristics of a new type of thermal interface materials, consisting of metal/elastomer interpenetrating phase composites. The 3D, highly porous copper scaffolds are fabricated via a fast and simple in situ bubble-templated electrodeposition process without the presence of solid templates; subsequently, the void fraction of the composite is filled by elastomer infiltration. The presence of elastomer matrix demonstrates limited impact on the thermal conductivity of the composite while it contributes substantially to the mechanical properties, providing the structural flexibility required. Thermal resistance values of 1.2–4.0 cm^2 K W^{-1} are measured upon multiple thermal cycles, confirming the mechanical stability of the composite, without showing any noticeable degradation.
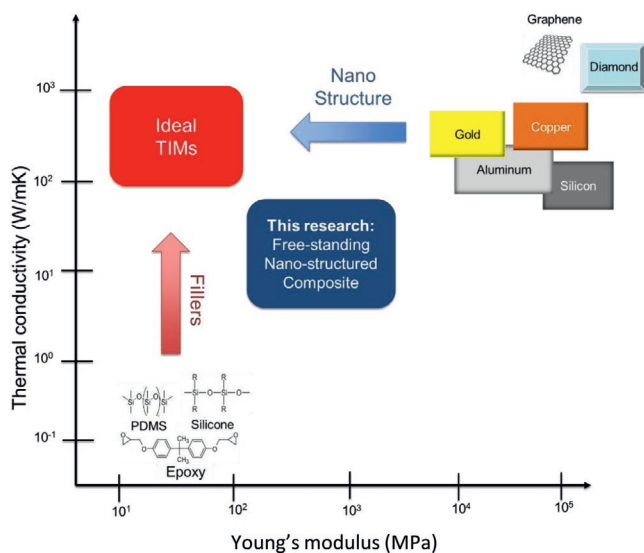
1. Introduction

With recent advances in semiconductor technology, the power density of electronic devices continues to escalate, urgently requiring the development of advanced thermal management solutions. Among many thermal management components in electronic packaging, thermal interface materials (TIMs) are essential in providing an effective conduction pathway between heat sources and heat sinks, thus they can maintain acceptable operating temperatures and avoid thermal-related breakdowns.[1,2] TIMs not only functionally serve as effective heat dissipation media but also accommodate thermal expansion

mismatch between two rigid surfaces as an intermediary layer.[3] Therefore, an ideal TIM should possess both low thermal resistance for efficient thermal transport as well as excellent mechanical compliance to accommodate strain mismatches upon thermal cycling. Typical TIMs, such as thermoplastic polymers, metals, and ceramics,[4,5] often fail to fulfill these two characteristics, either due to the high stiffness (or low mechanical compliance) of metals or the low thermal conductivity of polymers (which is typically lower than 0.4 W m^{-1} K^{-1})[6,7] (**Figure 1**). Therefore, it has been a topic of great interest to engineer thermally conductive polymer composites for the use in TIMs.

One possible approach is to disperse thermally conductive micro/nano-scale fillers (e.g., SiC, Al_2O_3, Ag, and graphene)[8–12] into the polymer matrix to enhance the effective thermal conductivity of the composite. In this approach, carbon-based fillers, such as carbon nanotubes, graphene nanoplatelets, or few layer graphene, have drawn significant attention due to their ultra-high intrinsic thermal conductivity, ranging from 3000 to 6600 W m^{-1} K^{-1}.[13–15] Various types of carbon-based TIMs have been demonstrated in previous studies[16,17] for this purpose. The random dispersion of carbon-based fillers causes discontinuity between heat transfer conduits, where the high loading fraction of fillers (usually over 50 vol%[18]) is suggested to minimize the discontinuity. The filling materials, however, increase the stiffness of the composite as well as compromise the mechanical integrity upon thermal cycling.[10,19] To address this issue, magnetic conductive fillers are employed and aligned under a force field during fabrication, eventuating in a 150% higher thermal conductivity than that of randomly dispersed fillers with a given filler volume ratio.[20] Despite some improvements,[21] the presence of additional thermal contact resistances between thermal filler particles is inevitable,[18,22] which might dominate the upper limit of the effective thermal conductivity.

An alternative approach is to demonstrate monolithic high-conductivity structures with continuous geometry. The use of continuous monolithic structure minimizes filler-filler contact resistances, enabling a higher thermal conductivity.[23–25] The monolithic structures are often fabricated by backfilling the vacancies of a sacrificial template with a desired structural material, the structure with

C.-H. Lin, A. Guell Izard, Prof. Y. Won
Department of Mechanical and Aerospace Engineering
University of California
Irvine, CA 92697, USA
E-mail: won@uci.edu
Prof. L. Valdevit
Department of Material Science and Engineering
University of California
Irvine, CA 92697, USA

The ORCID identification number(s) for the author(s) of this article can be found under https://doi.org/10.1002/admi.202001423.

**ADVANCED
SCIENCE NEWS**
www.advancedsciencenews.com

**ADVANCED
MATERIALS
INTERFACES**
www.advmatinterfaces.de

Figure 1. Dispersion of thermally conductive fillers and fabrication of nano structures are the most common strategies implemented to increase thermal conductivity and mechanical flexibility for polymer-based and metal-based thermal interface materials (TIMs), respectively. In this study, the combination of those two strategies is adopted. The free-standing porous copper/elastomer interpenetrating phase composite (IPC) aims to attain both high thermal conductivity and polymer-like mechanical properties.

inverse-morphology of the template is then formed. After the formation of the structural material, sacrificial templates are then typically etched or dissolved by using suitable chemistry.[26–29] The process of the sacrificial template formation and removal results in additional fabrication costs and byproducts. To minimize those issues, our study adopts in situ bubble-templated electrodeposition to create 3D metal foam.[30–32] Here, hydrogen bubbles are continuously and dynamically generated under high electrochemical potentials, serving as templates. The synchronized electrodeposition enables the fabrication of an interconnected, highly porous, and foam-like 3D biporous copper (BPCu). While previous researches have investigated the two-phase thermofluidic characteristics (e.g., boiling heat transfer enhancements) using porous copper,[33–38] the potential use of these materials in the form of metal/elastomer interpenetrating phase composites (IPCs) for TIMs applications remains unexplored.

In this work, we demonstrate a new type of free-standing, 3D porous copper structure by employing a fast and facile fabrication method, the in situ bubble-templated electrodeposition. Once porous copper structures are prepared, polydimethylsiloxane (PDMS) elastomer is infiltrated into the metal matrix, resulting in BPCu/PDMS IPCs. Owing to the combination of elastomer and porous copper, BPCu/PDMS IPCs not only preserve polymer-like mechanical properties but also show high thermal conductivities through the continuous structural backbone consisting of electrodeposited metal (Figure 1). Here, the thermal and mechanical properties of the BPCu/PDMS IPCs are characterized for various operating conditions, including repetitive thermal cycling, to confirm their reliable and durable performances.

2. Results and Discussion

2.1. Bubble-Templated Morphology

The free-standing biporous copper/polydimethylsiloxane (BPCu/PDMS) IPCs are fabricated using a combination of substrate preparation, in situ bubble-templated electrodeposition, and PDMS infiltration in series, as illustrated in Figure S1, Supporting Information. The details of the fabrication process are explained in the Experimental Section and the Supporting Information. The SEM images of as-fabricated BPCu structures and BPCu/PDMS IPCs are shown in **Figure 2**. Here, the top view of the as-fabricated BPCu structures with 1–3 min deposition time confirms a foam-like, 3D interconnected porous morphology with micro- and nanoscale features (Figure 2a–c). The average structure thickness is measured based on the cross-sectional SEM images, as displayed in **Figure 3**e. It should be noted that the structure thickness is used to nominate each BPCu structure in the following paragraphs. Therefore, 150, 340, and 520 BPCu structures indicate the structures after 1-, 2-, and 3-min electrodeposition, respectively.

During the fabrication process, hydrogen bubbles are formed around the cathode and the substrate under a high current density. Many small-sized bubbles are generated at the substrate surface and coalesce into larger bubbles as they depart the surface. The nature of the bubble generation facilitates a gradient pore morphology in the out-of-plane direction. For example, as the deposition time increases, the pore size increases with a smaller pore density on the top side, as shown in Figure 2d–f. The existence of a gradient morphology is supported by additional high magnification SEM images in Figure S2, Supporting Information, and elsewhere.[31,33] Similarly, the pore diameter increases with increasing deposition time. In Figure 3a–c, the pore diameter is in the range of several micrometers to 100 μm, with the peak in the 0–20 μm range for the 150 BPCu structure. For 340 and 520 BPCu samples, the peaks range from 150 to 170 μm and from 150 to 190 μm, respectively. This corresponds to the average pore diameters of 27.6, 134.7, and 160.4 μm for 1-, 2-, and 3-min deposition time, as shown in Figure 3d. Inversely, the pore number density decreases (Figure 3d) as the bubbles coalesce into larger bubbles during the bubble generation process.

In addition to the pore morphology, we further calculate the structural porosity by considering the average structure thickness and mass of the BPCu structures (Table S1, Supporting Information):[37]

$$\varnothing = 1 - \frac{m}{\rho \delta A_{\text{proj}}} \tag{1}$$

where m is the net mass of the BPCu structure, ρ is the copper density, δ is the average structure thickness, and A_{proj} is the projected area of BPCu structure. The porosities are calculated as 90.1–92.4% (orange markers in Figure 3e), where the values of the structural porosity are consistent with previously reported values.[37,39] Because of the large structural porosity, as-fabricated BPCu structures are generally fragile against mechanical stress, which requires further mechanical reinforcement, such as PDMS infiltration in this study. After the PDMS infiltration process, the corresponding values of the average structural thickness of
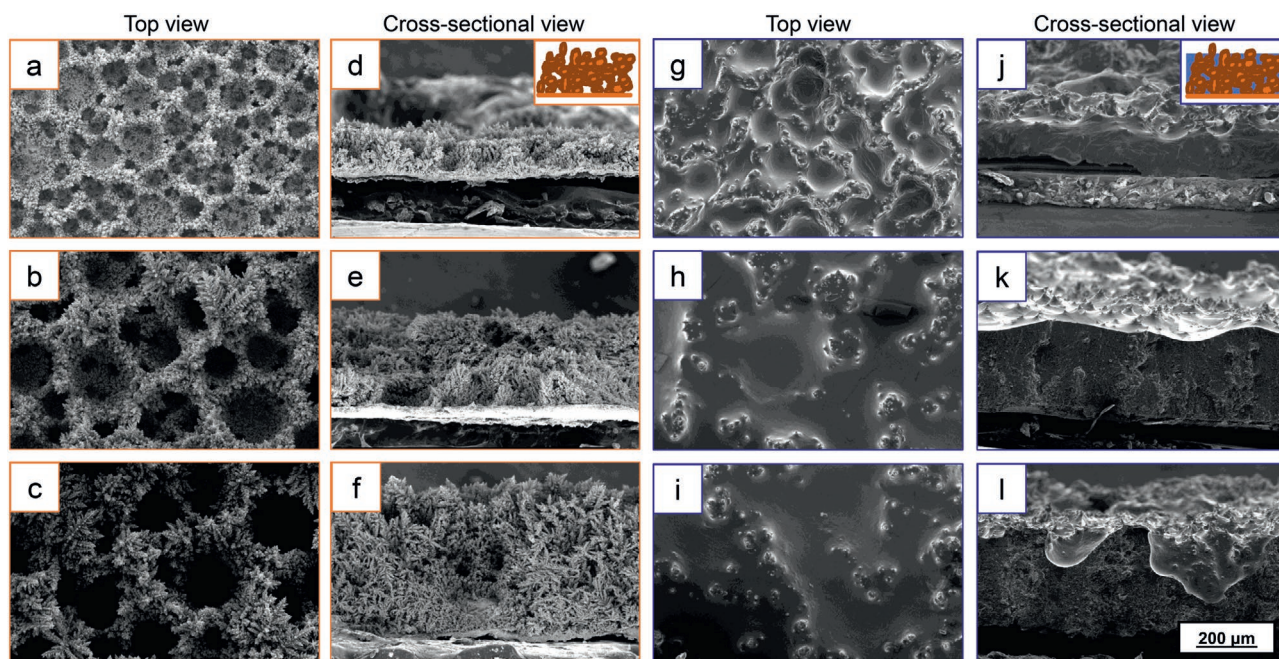
Figure 2. a–c) Top and d–f) cross-sectional SEM images of 150, 340, and 520 BPCu structures. The 3D interconnected, foam-like porous structures are created by dynamically formed hydrogen bubbles, as illustrated in the inset. The average structure thickness increases as the deposition time increases. g–i) Top and j–l) cross-sectional SEM images of 150, 340, and 520 BPCu/PDMS IPCs. Cross-sectional images confirm that PDMS matrix can penetrate through porous copper down to the bottom layer.
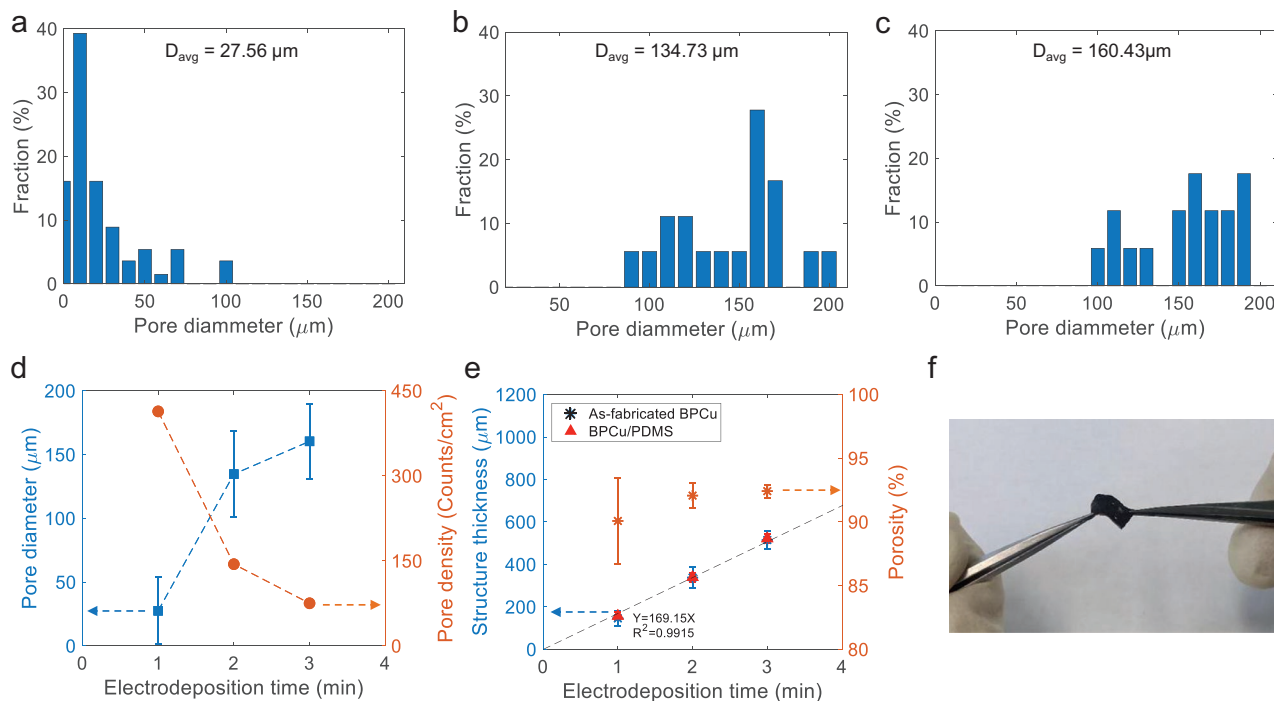
Figure 3. Pore diameter distribution of a) 150, b) 340, and c) 520 BPCu structures. The average pore diameter measured from the top images increases when the deposition time increases from 1 to 3 min. d) The average pore size distribution and pore density per unit area with respect to the electrodeposition time. When the deposition time increases, the multiple bubbles coalesce into large bubbles, increasing the average pore size and decreasing the pore number density. e) The structure thicknesses of the as-fabricated BPCu structures and BPCu/PDMS IPCs. The structure thickness distributions of both groups show similar linear trend versus deposition time. The structural porosity slightly increases from 90.1% to 92.4% when the deposition time increases from 1 to 3 min. f) The free-standing BPCu/PDMS IPC is successfully developed, with the structural flexibility.
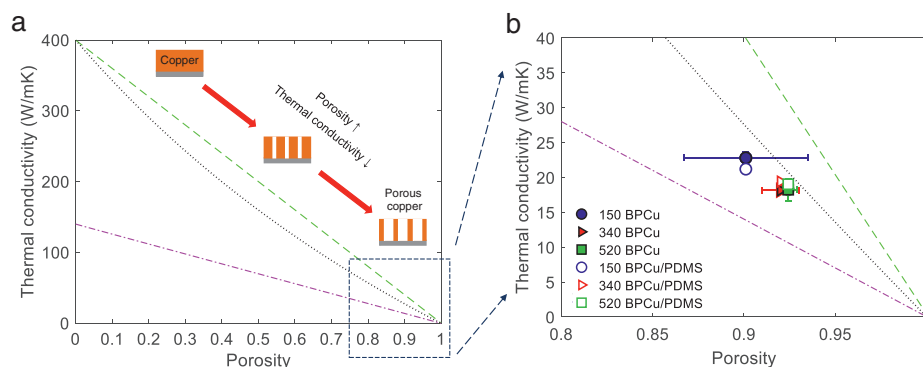
Figure 4. a,b) Theoretical thermal conductivity as a function of structural porosity by using three different models including volume fraction scaling model, Maxwell, EMT model, and empirical metal foam model. Volume fraction scaling model and Maxwell's EMT model overestimate the effective thermal conductivity as they simplify the porous structures. The empirical metal foam model estimates the effective thermal conductivity of commercial metal foam. The upper and lower limits of the effective thermal conductivities of porous structures with a given porosity are suggested in the models; however, they do not fully account for the morphological details.

BPCu/PDMS IPCs (red markers in Figure 3e) are similar to those of the BPCu counterparts. The consistent values of thickness confirm that the PDMS effectively penetrates through the entire BPCu structure. The elastomer thickness is controlled not to deposit beyond the BPCu's thickness, as evidenced in Figure 2g–l.

2.2. Effective Thermal Conductivity

The effective thermal conductivity quantitatively explains how much heat can be dissipated through metal/elastomer composites. For this, the temperature gradient across the composites described in Figure S4, Supporting Information, is used to calculate the in-plane thermal conductivity of the sample. The thermal conductivity of BPCu structures is measured to be 18.2–22.8 W m^{-1} K^{-1}, whereas that of BPCu/PDMS IPCs is 19.0–21.2 W m^{-1} K^{-1}, as shown in **Figure 4** and **Table 1**. This confirms that the PDMS infiltration process has the minimal impact on the effective thermal conductivity of BPCu/PDMS IPCs, and the conduction pathways of BPCu structures can be preserved even after the PDMS infiltration. During the fabrication process of BPCu, the coalescence events of hydrogen bubbles create a gradient pore morphology along the through-plane direction, as showcased in Figure 3. The porosity of BPCu is independent of time and remains as a constant, where the minimum dendrite features (≈100–200 nm) are much larger than the mean free path of copper (≈40 nm),[40] suggesting the direction-independent, constant thermal conductivity. Therefore, we assume that the effective thermal conductivities of as-fabricated BPCu structures and BPCu/PDMS IPCs are identical in both through-plane and in-plane directions, in this study.

The measured thermal conductivities are compared to the values calculated by theoretical models, such as the volume fraction scaling model,[41] Maxwell's effective mean theory (EMT) model,[28,42] and the empirical foam model.[43] The models estimate the effective thermal conductivity of porous structures as a function of structural porosity ø by suggesting the upper or lower limits depending on their pore morphology. The volume fraction scaling model expresses the effective conductivity k_{eff} as:

$$k_{eff} = k_{PDMS} \varnothing + k_{Cu}(1-\varnothing) \quad (2)$$

where k_{PDMS} is the thermal conductivity of PDMS (k_{PDMS} = 0.4 W m^{-1} K^{-1}), and k_{Cu} is the thermal conductivity of the pure copper (k_{Cu} = 400 W m^{-1} K^{-1}). The volume fraction scaling model estimates a thermal conductivity of 30.8–40.0 W m^{-1} K^{-1} for 90.1–92.4% porosity. This model suggests the upper bound of the estimated thermal conductivity because the model ignores the structural tortuosity of 3D porous structures by simply accounting for parallel thermal resistances of the two materials.[42]

The Maxwell's EMT model has been typically used in previous studies to estimate the effective thermal conductivity of nanostructured structures containing close-packed spherical pores:[44,45]

$$k_{eff} = \left(\frac{2(1-\varnothing)}{3-(1-\varnothing)} \right) k_{Cu} \quad (3)$$

This model overestimates the effective thermal conductivity (≈20.8–27.4 W m^{-1} K^{-1}) since the overall structural porosity of our case surpasses the close-packed limit $\varnothing \approx 65\%$.[46,47]

Table 1. Effective thermal conductivity of as-fabricated BPCu structures and BPCu/PDMS IPCs.

	150 BPCu	150 BPCu/PDMS	340 BPCu	340 BPCu/PDMS	520 BPCu	520 BPCu/PDMS
q_1'' [kW m^{-2}]	5.33	6.67	13.33	10.68	13.33	16.00
ΔT_{BPCu} [°C]	27.30	36.70	37.80	28.30	24.60	28.30
k [W m^{-1} K^{-1}]	22.79	21.19	18.16	19.40	18.24	19.03
Deviation [%]		−7.02		6.39		4.15

**ADVANCED
SCIENCE NEWS**

www.advancedsciencenews.com

**ADVANCED
MATERIALS
INTERFACES**

www.advmatinterfaces.de

The empirical metal foam model might provide the lower bound of thermal conductivities, where this model is valid for foam-like structures with a ultra-high porosity range of 90.5–97.8% and a large pore size of 300–500 μm:[48]

$$k_{eff} = A \left(k_{PDMS}\emptyset + k_{Cu}(1-\emptyset) + \left(\frac{1-A}{\frac{\emptyset}{k_{PDMS}} + \frac{1-\emptyset}{k_{Cu}}} \right) \right) \quad (4)$$

where $A = 0.35$ is an empirical coefficient. The calculated effective thermal conductivities of the BPCu/PDMS samples are in the range of 11.4–14.2 W m^{-1} K^{-1}. Although the theoretical or empirical models provide the upper and lower bounds, it is challenging to accurately estimate the effective thermal conductivity of nano or microstructured materials because of morphological deviations between theoretical models and the BPCu structures.

2.3. Mechanical Strength Enhancement by PDMS Infiltration

Tensile tests are performed to quantify the mechanical properties of the BPCu/PDMS IPC. Stress-strain curves of the two constituent materials (i.e., copper and PDMS) and the BPCu/PDMS IPC under uniaxial tension are displayed in **Figure 5**, where the insets show the samples tested. Figure 5a describes the tensile stress-strain response of the copper film, clearly displaying brittle behavior. Tensile strength $\sigma_{t\,Cu}$ and Young's modulus E_{Cu} of the copper film are measured to be 250 MPa and 94 GPa, respectively, while the tensile failure occurs at strain $\varepsilon_{t\,Cu} = 0.6\%$. For the PDMS film, the tensile strength $\sigma_{t\,PDMS}$ and the initial Young's modulus E_{PDMS} are measured to be 0.3 MPa and 1.6 MPa, with tensile failure occurring at $\varepsilon_{t\,PDMS} = 71.0\%$ (Figure 5b). Figure 5c shows the tensile stress-strain curve of the BPCu/PDMS IPC, from which $\sigma_{t\,BPCu/PDMS}$ and $E_{BPCu/PDMS}$ are extracted as 0.8 MPa and 141 MPa, respectively. Note that the stress-strain curve of the BPCu/PDMS presents two failure points during tensile loading, indicating that the copper ligaments and the PDMS matrix do not break simultaneously during the test. Initially, the sample fails in a brittle manner at a strain $\varepsilon_{t\,BPCu/PDMS} = 0.8\%$ and a strength $\sigma_{t\,BPCu/PDMS} = 0.8$ MPa, which corresponds to the rupture of copper structure. Subsequently, the remaining PDMS matrix and copper dendrite break at a tensile strain $\varepsilon_{t\,BPCu/PDMS} = 5.5\%$ and a strength $\sigma_{t\,BPCu/PDMS} = 0.3$ MPa.

The Voigt and Reuss bounds[49] evaluate the upper and lower limits of the Young's modulus for the BPCu/PDMS IPC. For the Voigt bounds, the Young's modulus of composites is calculated by assuming the strain equality of each material, so the calculated modulus is considered as the upper limits for the composites and follows the volume fraction scaling:

$$E_{eff} = E_{PDMS}\,\emptyset + E_{Cu}(1-\emptyset) \quad (5)$$

where E_{PDMS} and E_{Cu} are the measured Young's modulus of PDMS and copper films, respectively, suggesting the calculated modulus in the range of 7.6–9.9 GPa for our case.

On the other hand, the Reuss bound represents the lower limit and postulates that each material of the composite shares the same stress, and the expression of the Young's modulus becomes:

$$E_{eff} = \frac{E_{PDMS}E_{Cu}}{E_{PDMS}\emptyset + E_{Cu}(1-\emptyset)} \quad (6)$$

The Reuss bound estimates the Young's modulus of the composite in the range from 16.2 to 21.1 MPa. The measured $E_{BPCu/PDMS}$ ranges between the upper and lower bounds. The measured mechanical properties of BPCu/PDMS IPCs, $E_{BPCu/PDMS}$ and $\sigma_{t\,BPCu/PDMS}$, are shown to be similar to the properties of a polymer.[50]

2.4. Pressure-Dependent Thermal Characteristics and Thermal Stability

To understand the overall performance of TIMs, the total thermal interface resistance R''_{total} of the BPCu/PDMS IPCs is measured by using a steady-state, 1D thermal conduction method, as explained in **Figure 6**a and Figure S3, Supporting Information. Applied pressure deforms the interface material and increases contact points between the mating surfaces, minimizing the amount of air gaps remaining at the interface, therefore decreasing the thermal contact resistance. The study of thermal transport is performed by applying pressures ranging from 0.5 to 2 MPa to capture pressure-dependent characteristics. We repeat the measurements of each sample for three times, to report the average values with standard deviations (that are indicated with error bars in the plots). The measurements indicate that thermal resistances R''_{total}
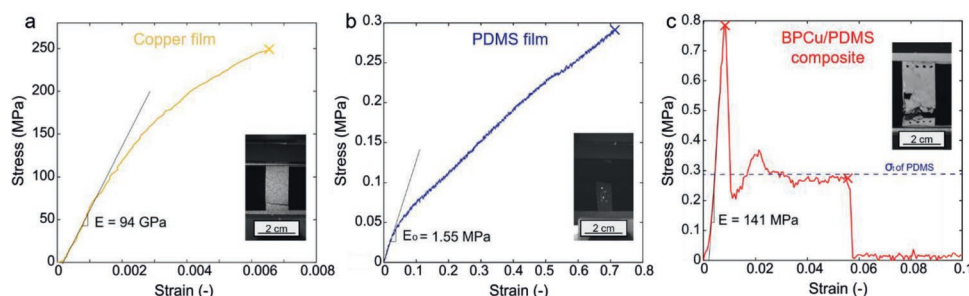
Figure 5. Stress-strain curves for a) copper film, b) PDMS film and c) BPCu/PDMS IPC. The first stress drop in the BPCu/PDMS IPC curve is associated with fracturing of the copper ligaments, with the final catastrophic drop at 6% strain corresponding to PDMS failure. Notice that the measured Young's modulus of BPCu/PDMS is three orders of magnitude lower than that of the copper film.
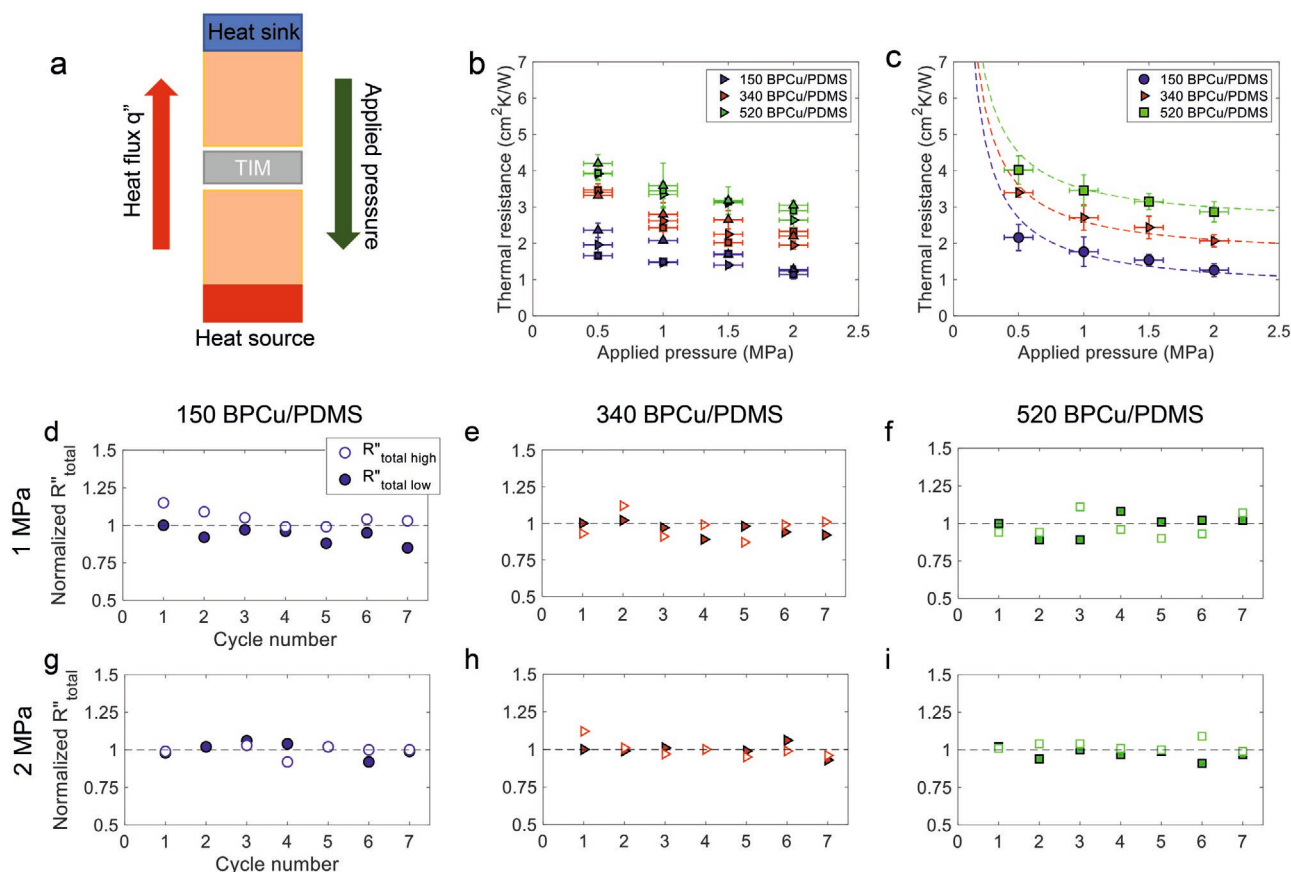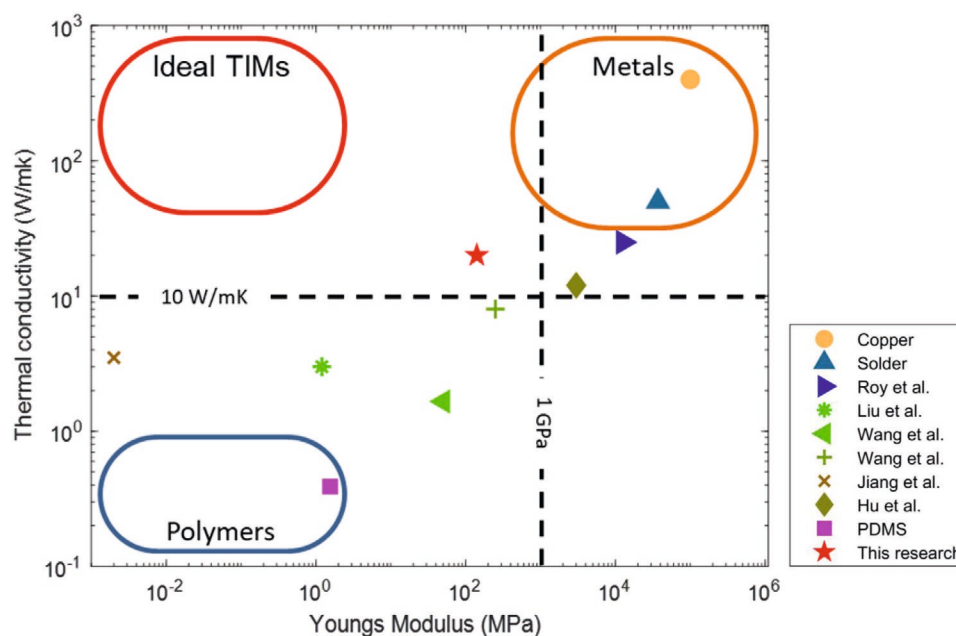
Figure 6. a) The schematic of pressure-dependent thermal resistance measurement. The tested sample is sandwiched by two symmetric copper bars which are connected to the heat source (bottom) and heat sink (top), respectively. The pressure is applied from the top of the apparatus and quantified by load cells. b) Measured thermal resistances R''_{total} under three individual measurements. c) Pressure-dependent thermal resistances of 150, 340, and 520 BPCu/PDMS IPCs. As the pressure increases, the thermal resistance decreases. Normalized thermal resistances $\frac{R''_{total}}{(\overline{R''_{total}})}$ of 150, 340, and 520 BPCu/PDMS IPCs during thermal cycle test under d–i) 1 MPa, f–h) 2 MPa applied pressure. After seven thermal cycles, no degradation is observed. Under higher applied pressure, average thermal resistance deviation is lower, which represents more consistent R''_{total} values, confirming the time-dependent reliability of samples.

decreases with smaller structural thickness (Figure 6b) or larger applied pressures (Figure 6c). The regression model estimates the thermal resistance as a function of applied pressure: $R''_{total} = CP^{-1} + Y$ where the fitting parameter C is 1.1 for all cases, and the offset Y in the y-direction is 0.7, 1.6, and 2.5 for 150, 340, and 520 BPCu/PDMS IPCs, respectively. The values of C and Y demonstrate the similar sensitivity of three composite groups under elevated pressures and regular total thermal resistance increments with respect to structure thickness increments. The R''_{total} under 0.5 MPa ranges from 2.2 to 4.0 cm² K W⁻¹ and decreases to 1.8–3.5 cm² K W⁻¹ when the pressure increases to 1 MPa. The average R''_{total} decreases by 12.7% and 12.0% when the pressure further increases from 1 to 1.5 and 2 MPa, respectively. The R''_{total} is less sensitive to the applied pressure in the high-pressure regime (≥1.5 MPa), as copper nanostructures are compressed and densified under the pressures, which also facilitates more contacts between BPCu/PDMS IPCs and the copper bar with smaller error bars. Figure 6c indicates that the error bars of R''_{total} (average thermal resistance deviations) in the low-pressure regime are 0.3–0.4 cm² K W⁻¹, and decrease down to 0.2 cm² K W⁻¹ with a applied pressure of 2.0 MPa.

In real application, TIMs often undergo multiple thermal cycles, which could deteriorate their performance and increase the total thermal resistance. This explains that the thermal stability of TIMs is another essential characteristic for performance evaluation. Therefore, the study of thermal transport is extended to thermal cycling conditions to confirm the thermal stability of the composites. The thermal stability is further discussed by using two input powers that generate different temperature gradients across the interface (Figure S5, Supporting Information). Herein, we obtain the R''_{total} of BPCu/PDMS IPCs under two applied pressures of 1 and 2 MPa during seven thermal cycles. The average $\overline{R''_{total}}$ during thermal cycles ranges from 1.4 to 3.2 cm² K W⁻¹ depending on their applied pressure or structure thickness. We normalize the individual R''_{total} over $\overline{R''_{total}}$ to quantify the thermal resistance variation of each thermal cycle. Figure 6d–i shows the normalized thermal resistance distribution during thermal cycling, with the solid and hollow markers representing R''_{total} measured under low and high input power,

ADVANCED
SCIENCE NEWS
www.advancedsciencenews.com

ADVANCED
MATERIALS
INTERFACES
www.advmatinterfaces.de

Figure 7. Comparison of thermal conductivity and Young's modulus between BPCu/PDMS IPC and other types of composite TIMs by past studies. The BPCu/PDMS shows polymer-like mechanical property without severe compromise in thermal conductivity.

respectively. It should be noted that the degree of fluctuation of the thermal resistance values during the cycling by using the definition of variation over multiple cycles:

$$\text{Variation} = \left| \frac{R''_{\text{total}}}{R''_{\text{total}}} - 1 \right| \tag{7}$$

For all cases, we do not observe any significant changes in the variations despite repetitive thermal cycles. As the applied pressure increases from 1 to 2 MPa, the average deviations for the BPCu/PDMS IPCs decrease significantly from 5.6% to 3.0%, and the maximum deviations decrease from 14.3% to 10.0%. This shows a good agreement with the small deviations in total thermal resistances with higher applied pressure.

The thermal and mechanical performances of the BPCu/PDMS IPCs are compared with other composite TIMs explained in previous work[51–56] (**Figure 7**). Even though the volume ratio of the conductive fillers is reduced via better filler alignment introduced by self-assembly or continuous framework, the composite TIMs in previous works still show limited thermal conductivity improvement (below 10 W m^{-1} K^{-1}) because of the thermal resistance between fillers. The employment of low melt alloys (LMAs) guarantees the high thermal conductivity, but the excessive increase in the Young's modulus (over 1 GPa) is observed due to the insufficient flexible phase. On the other hand, by combining the continuous heat transfer pathway and flexible elastomer matrix, BPCu/PDMS IPCs show polymer-like mechanical property while retaining a reasonable thermal conductivity.

3. Conclusion

In summary, we demonstrate a new classification of copper polymer composites, called the BPCu/PDMS IPCs through

in situ bubble-templated electrodeposition. The electrodeposition facilitates the formation of monolithic metal structures around the bubble template, which can significantly reduce particle-to-particle thermal contact resistances. The following elastomer infiltration is suggested to improve the structural reliability of the copper polymer composites, enabling more polymer-like mechanical characteristics. Also, the composites preserve the porous copper's thermal conductivity of 20 W m^{-1} K^{-1}, which is independent to the elastomer infiltration. The thermal characteristic measurements of BPCu/PDMS IPCs are performed and further extended to thermal cycling conditions, which demonstrate thermal stability of the composites is also confirmed, showing no prominent degradation under the thermal cycling conditions. The unique combination of thermal and mechanical characteristics of the BPCu/PDMS IPCs suggests the use in TIMs or packaging applications.

4. Experimental Section

Fabrication of Free-Standing BPCu/PDMS Interpenetrating Phase Composites: The fabrication process of free-standing BPCu/PDMS IPCs consisted of substrate preparation, bubble-templated electrodeposition, and elastomer infiltration in series, as illustrated in Figure S1, Supporting Information. The polystyrene (PS) sheet with a thickness of 1 mm was cut into 20 mm × 15 mm rectangular substrates. The substrates were placed in isopropyl alcohol (IPA) and ultrasonicated for 20 min. The electron beam evaporator (EvoVac Glovebox Evaporator, Angstrom Engineering Inc., U.S.) was employed to coat a 100 nm copper thin film on the top surface of the polystyrene (PS) substrate with 2.0 Å s^{-1} coating rate. The thickness of an as-coated copper film was further increased under Galvanostatic electrodeposition process in the three-electrode electrochemical cell with constant current set to be 28.8 mA versus Ag/AgCl for 40 min, and the process was conducted in the stationary 0.5 M Cu$_2$SO$_4$ + 0.1 M H$_2$SO$_4$ electrolyte. The electrodeposited substrates were placed

in organic solvent for 12 h to fully dissolve PS substrate, which enabled the free-standing copper films with a thickness of ≈10 µm. For the bubble-templated electrodeposition, the deposited area was set to be 10 mm × 10 mm, so Kapton tape was utilized to designate deposited area on the copper films. The copper films were assembled with the customized polycarbonate (PC) holder and attached to the cathode, while a copper sheet of 15 mm × 10 mm served as an anode. The substrate and the electrode were placed horizontally with the vertical distance between anode and cathode set to 35 mm. The bubble-templated electrodeposition was performed in 0.4 M Cu_2SO_4 + 1.8 M H_2SO_4 electrolyte with current density to be 1.0 A cm^{-2}. As a by-product of the process, hydrogen bubbles were dynamically and continuously generated during the process and served as a template to create void portions within the deposited copper. The thicknesses of as-fabricated BPCu structures were controlled by altering the electrodeposition time ranging from 1 to 3 min. After the electrodeposition, as-fabricated BPCu structures were cleaned with deionized water and dried. For the mechanical strength enhancement, as-fabricated BPCu structures was then infiltrated with elastomer matrix. A low viscosity PDMS (Sylgard 170, Dow Corning Inc., U.S., thermal conductivity k_{PDMS} = 0.4 W m^{-1} K^{-1}, service temperature = −45 to 200 °C, viscosity v = 2675 mPa s) was mixed with 1:1 volume ratio between elastomer base and curing agent. The casting area of BPCu was confined with tapes, and the PDMS was drop-cast on the BPCu structures. The wicking effect of the BPCu structure would spread the PDMS throughout the entire deposited area, and after curing for 24 h at room temperature, a free-standing BPCu/PDMS IPC was developed. The statistics of pore morphology were analyzed by post-processing the micrographs via ImageJ.

Infrared Image-Based Effective In-Plane Thermal Conductivity Measurement: The measurement of effective in-plane thermal conductivity was conducted by quantifying the net heat flux q''_1 and recording the temperature gradient cross tested samples ΔT_{BPCu}. As shown in Figure S4, Supporting Information, the tested samples (i.e., as-fabricated BPCu structures and BPCu/PDMS IPCs) were connected to the reference copper sheet and heat sink, respectively, and a 1D thermal circuit in series was formed. The reference copper sheet of 35 mm × 12 mm × 0.5 mm was attached to the heat source, which served as the reference to calculate the q''_1 passing through the tested samples. Similar to the fabrication process introduced in the previous section, the bubble-templated electrodeposition on the PS sheet with copper seed layer of 12 and 40 mm was repeated. This time, the PS sheet was preserved for better sample rigidity. The emissivity in infrared region for each material was calibrated before measurements, and the emissivity values for each material were listed in Table S2, Supporting Information. According to the temperature difference of the reference copper sheet ΔT_{Cu}, the net heat flux q''_1 passing through the reference copper sheet could be calculated by the following equations:

$$\Delta T_{Cu} = q''_1 \frac{L_{Cu}}{k_{Cu}} \tag{8}$$

where the R''_{Cu} was calculated based on the measured length of copper sheet (L_{Cu} = 30 mm) and the thermal conductivity of reference copper sheet (k_{Cu} = 400 W m^{-1} K^{-1}). The heat losses through convection and radiation in this measurement were responsible 2.0% and 0.9% of the average q''_1, so the conduction through the thermal circuit remains the dominant heat transfer mechanism with the 1D heat transfer assumption. It was assumed that the total heat rate passing through the reference copper sheet and the samples could thus be regarded as equivalent, implying that the 3D BPCu structure could be considered the main heat transfer medium during the measurement. As the thermal conductivity of PS was 0.1 W m^{-1} K^{-1},[57] the heat transfer rate through PS layer was negligible. Therefore, the heat flux passing through the tested sample q''_2 could be expressed as:

$$q''_1 \quad Ac_{Cu} = q''_2 \quad Ac_{BPCu} \tag{9}$$

where the cross-sectional area Ac was width w × structure thickness δ, and both the reference copper sheet and the measured samples had the same w of 12 mm. Equation (10) could be be further reduced to:

$$q''_2 = q''_1 \frac{\delta_{Cu}}{\delta_{BPCu}} \tag{10}$$

The effective in-plane thermal conductivity of the as-fabricated BPCu structure and BPCu/PDMS IPC could finally be extracted as:

$$k_{BPCu} = q''_1 \frac{\delta_{Cu}}{\delta_{BPCu}} \frac{L_{BPCu}}{\Delta T_{BPCu}} \tag{11}$$

where the measured length of all tested samples L_{BPCu} was fixed as 35 mm.

Mechanical Characterization: Uniaxial tensile tests to characterize the mechanical response of BPCu/PDMS samples, as well as the two constituent materials were performed. The two constituent materials were electrodeposited copper and PDMS, both in film form. All samples had a width of 12 mm and length of 18 mm. The thickness of the copper film, PDMS film, and BPCu/PDMS film were 10 µm, 500 µm and 340 µm, respectively. The tensile tests were performed using a universal testing machine (Instron Inc., U.S., model 8862) at a strain rate of 0.1% s^{-1}. Viscoelastic effects in the elastomer were ignored. To facilitate clamping of samples in the tensile grips with minimal damage to the samples, the top and bottom ends of each samples were glued to poly (methyl methacrylate) (PMMA) plates. The load was measured by a load cell and converted to engineering (nominal) stress by dividing it by the undeformed cross-sectional area of the sample. The strain of the copper sample was extracted using 3D digital image correlation (VIC 3D, correlated solutions), while the strain of the other samples was obtained by tracking fiducial markers via a digital image correlation algorithm developed in house. The initial Young's modulus was extracted as the slope of the stress-strain curve at 0 strain, and the strength was defined as the maximum stress sustained by the sample before failure.

Pressure-Dependent Thermal Characterization: Pressure-dependent thermal properties of BPCu/PDMS IPCs were measured by using steady-state, 1D heat conduction method as specified in ASTM D5470-06. For this, the tested samples were placed between two symmetric square copper bars with 10 mm × 10 mm cross-sectional area, which were connected to heat source and heat sink, respectively. Liquid water, consisting of a water pump and two 4 mm inner diameter hoses, flowed through the upper copper bar as the heat sink, and two cartridge heaters (CIR-20191/120V, Omega Inc., U.S.) with an adjustable AC power supply were placed beneath the lower copper bar as the heat source. K-type thermocouples measure the temperature distribution in thermal equilibrium at three locations along two copper bars. Based on the 1D conduction assumption, the net heat flux q'' could be calculated by using the Fourier's Law:

$$q'' = -k_{Cu} \frac{dT}{dX} \tag{12}$$

where the temperature gradient $\frac{dT}{dX}$ was calculated average temperature gradient between three temperature points along the copper bars in thermal equilibrium.

To minimize, the influence of convective and radiative heat losses, ceramic blanket and Teflon block covered the exposed surfaces of copper bars. The convective heat transfer coefficient of free air and emissivity of copper bar set to be 10 W m^{-2} K^{-1} and 0.87, respectively, were assumed. The heat losses were calculated to be 940 and 765 W m^{-2} for convection and radiation, respectively, which were responsible for 7.8% and 6.4% of the average net heat flux q''. Therefore, the total interface resistance could be expressed as a series of thermal resistances $R''_{total} = R''_{Cu-Cu} + R''_{Cu} + R''_{TIM-Cu} + R''_{TIM}$, and the total thermal resistance could be calculated by dividing the temperature difference ΔT_{Sample} between top surfaces of upper and lower copper bars by the heat flux q'' passing through the thermal circuit. The uncertainty for measured R''_{total} based on the uncertainties of the primary quantities was also calculated. Uncertainties

**ADVANCED
SCIENCE NEWS**

www.advancedsciencenews.com

**ADVANCED
MATERIALS
INTERFACES**

www.advmatinterfaces.de

for K-type thermal couples, power input, and machining tolerance were ± 0.2 K, ± 1 W, and $\pm 10^{-4}$ m, respectively, and the calculated uncertainty on the measured R''_{total} was 2.1%. On the top layer of the apparatus, a threaded rod was installed for force exertion on the interface and four load cells were affixed in series for pressure quantification. The applied forces were chosen to be 50–200 N, which were equivalent to 0.5–2 MPa pressure exerted on 1 cm^2 area. Measurement validity verification was conducted after the apparatus was built, and the results were shown in the Supporting Information. To analyze and predict the pressure-dependent thermal characteristics of BPCu/PDMS IPCs, pressure-inverse functional form was adopted, and the relation between measured R''_{total} and applied pressure could be expressed as: $R''_{total} = CP^{-1} + Y$, where C represents the fitting parameter, P was the applied pressure, and Y was the equation offset in the y-direction.[24]

Supporting Information

Supporting Information is available from the Wiley Online Library or from the author.

Acknowledgements

Conflict of Interest

The authors declare no conflict of interest.

Keywords

[1] R. Prasher, *Proc. IEEE* **2006**, *94*, 1571.
[2] J. P. Gwinn, R. L. Webb, *Microelectron. J.* **2003**, *34*, 215.
[3] K. M. Razeeb, A. Munari, E. Dalton, J. Punch, S. Roy, in *Proc. of the ASME–SME Thermal Engineering Conf. and Summer Heat Transfer Conf.*, American Society of Mechanical Engineers, New York **2009**, pp. 817–823.
[4] A. S. Cherkasova, J. W. Shan, *J. Heat Transfer* **2008**, *130*, 082406.
[5] Z. Han, A. Fina, *Prog. Polym. Sci.* **2011**, *36*, 914.
[6] Y. Agari, T. Uno, *J. Appl. Polym. Sci.* **1986**, *32*, 5705.
[7] X. Huang, C. Zhi, P. Jiang, D. Golberg, Y. Bando, T. Tanaka, *Adv. Funct. Mater.* **2013**, *23*, 1824.
[8] Z. Shi, M. Radwan, S. Kirihara, Y. Miyamoto, Z. Jin, *Appl. Phys. Lett.* **2009**, *95*, 224104.
[9] C. Zhi, Y. Bando, T. Terao, C. Tang, H. Kuwahara, D. Golberg, *Adv. Funct. Mater.* **2009**, *19*, 1857.
[10] B. Tang, G. Hu, H. Gao, L. Hai, *Int. J. Heat Mass Transfer* **2015**, *85*, 420.
[11] K. M. F. Shahil, A. A. Balandin, *Nano Lett.* **2012**, *12*, 861.
[12] Y. H. Zhao, Z. K. Wu, S. L. Bai, *Composites, Part A* **2015**, *72*, 200.
[13] A. M. Marconnet, M. A. Panzer, K. E. Goodson, *Rev. Mod. Phys.* **2013**, *85*, 1295.
[14] S. Berber, Y.-K. Kwon, D. Tomanek, *Phys. Rev. Lett.* **2000**, *84*, 4613.

[15] A. A. Balandin, S. Ghosh, W. Bao, I. Calizo, D. Teweldebrhan, F. Miao, C. N. Lau, *Nano Lett.* **2008**, *8*, 902.
[16] W. Lin, K. S. Moon, C. P. Wong, *Adv. Mater.* **2009**, *21*, 2421.
[17] A. M. Marconnet, N. Yamamoto, M. A. Panzer, B. L. Wardle, K. E. Goodson, *ACS Nano* **2011**, *5*, 4818.
[18] F. Kargar, Z. Barani, R. Salgado, B. Debnath, J. S. Lewis, E. Aytan, R. K. Lake, A. A. Balandin, *ACS Appl. Mater. Interfaces* **2018**, *10*, 37555.
[19] R. Prasher, *Intel Technol. J.* **2005**, *09*, https://doi.org/10.1535/itj.0904.03.
[20] C. Yuan, B. Duan, L. Li, B. Xie, M. Huang, X. Luo, *ACS Appl. Mater. Interfaces* **2015**, *7*, 13000.
[21] J. Chen, X. Huang, B. Sun, Y. Wang, Y. Zhu, P. Jiang, *ACS Appl. Mater. Interfaces* **2017**, *9*, 30909.
[22] L. E. Nielsen, *Ind. Eng. Chem. Fundam.* **1974**, *13*, 17.
[23] M. T. Barako, S. Roy-Panzer, T. S. English, T. Kodama, M. Asheghi, T. W. Kenny, K. E. Goodson, *ACS Appl. Mater. Interfaces* **2015**, *7*, 19251.
[24] M. T. Barako, S. G. Isaacson, F. Lian, E. Pop, R. H. Dauskardt, K. E. Goodson, J. Tice, *ACS Appl. Mater. Interfaces* **2017**, *9*, 42067.
[25] J. Xu, A. Munari, E. Dalton, A. Mathewson, K. M. Razeeb, *J. Appl. Phys.* **2009**, *106*, 124310.
[26] C. Zhang, J. W. Palko, M. T. Barako, M. Asheghi, J. G. Santiago, K. E. Goodson, *Adv. Funct. Mater.* **2018**, *28*, 1803689.
[27] C. Zhang, G. Rong, J. W. Palko, T. J. Dusseault, M. Asheghi, J. G. Santiago, K. E. Goodson, in *ASME 2015 Int. Technical Conf. and Exhibition on Packaging and Integration of Electronic and Photonic Microsystems, InterPACK 2015, Collocated with the ASME 2015 13th Int. Conf. on Nanochannels, Microchannels, and Minichannels*, American Society of Mechanical Engineers, New York **2015**.
[28] C. Zhang, J. W. Palko, G. Rong, K. S. Pringle, M. T. Barako, T. J. Dusseault, M. Asheghi, J. G. Santiago, K. E. Goodson, *ACS Appl. Mater. Interfaces* **2018**, *10*, 30487.
[29] J. H. Ha, E. Oh, I. H. Song, *J. Ceram. Soc. Jpn.* **2013**, *121*, 940.
[30] H. C. Shin, J. Dong, M. Liu, *Adv. Mater.* **2003**, *15*, 1610.
[31] H. C. Shin, M. Liu, *Chem. Mater.* **2004**, *16*, 5460.
[32] V. D. Patake, S. S. Joshi, C. D. Lokhande, O. S. Joo, *Mater. Chem. Phys.* **2009**, *114*, 6.
[33] S. Li, R. Furberg, M. S. Toprak, B. Palm, M. Muhammed, *Adv. Funct. Mater.* **2008**, *18*, 2215.
[34] A. Jaikumar, S. G. Kandlikar, *Int. J. Heat Mass Transfer* **2016**, *95*, 795.
[35] A. M. Gheitaghy, H. Saffari, D. Ghasimi, A. Ghasemi, *Appl. Therm. Eng.* **2017**, *113*, 1097.
[36] A. M. Rishi, A. Gupta, S. G. Kandlikar, *Appl. Therm. Eng.* **2018**, *140*, 406.
[37] Y. Q. Wang, J. L. Luo, Y. Heng, D. C. Mo, S. S. Lyu, *Int. J. Heat Mass Transfer* **2018**, *119*, 333.
[38] J. Li, W. Fu, B. Zhang, G. Zhu, N. Miljkovic, *ACS Nano* **2019**, *13*, 14080.
[39] P. Xu, Q. Li, Y. Xuan, *Int. J. Heat Mass Transfer* **2015**, *80*, 107.
[40] V. V. R. Narasimha Rao, S. Mohan, P. J. Reddy, *J. Phys. D: Appl. Phys.* **1976**, *9*, 89.
[41] J. Wang, J. K. Carson, M. F. North, D. J. Cleland, *Int. J. Heat Mass Transfer* **2006**, *49*, 3075.
[42] M. T. Barako, A. Sood, C. Zhang, J. Wang, T. Kodama, M. Asheghi, X. Zheng, P. V. Braun, K. E. Goodson, *Nano Lett.* **2016**, *16*, 2754.
[43] A. Bhattacharya, V. V. Calmidi, R. L. Mahajan, *Int. J. Heat Mass Transfer* **2002**, *45*, 1017.
[44] S. Datta, C. T. Chan, K. M. Ho, C. M. Soukoulis, *Phys. Rev. B* **1993**, *48*, 14936.
[45] H. T. Aichlmayr, F. A. Kulacki, *Adv. Heat Transfer* **2006**, *39*, 377.
[46] J. Canny, *IEEE Trans. Pattern Anal. Mach. Intell.* **1986**, *PAMI-8*, 679.
[47] R. B. Bird, W. E. Stewart, E. N. Lightfoo, *Transport Phenomena*, John Wiley and Sons, Inc., New York **1960**.
[48] L. Zhang, K. Zhou, Q. Wei, L. Ma, W. Ye, H. Li, B. Zhou, Z. Yu, C. TeLin, J. Luo, X. Gan, *Appl. Energy* **2019**, *233–234*, 208.
[49] M. F. Ashby, *Metall. Ital.* **1994**, *86*, 475.
[50] J. R. Ebdon, *Polym. Int.* **1993**, *30*, 281.

[51] C. K. Roy, S. Bhavnani, M. C. Hamilton, R. W. Johnson, J. L. Nguyen, R. W. Knight, D. K. Harris, *Int. J. Heat Mass Transfer* **2015**, *85*, 996.

[52] J. Liu, M. O. Olorunyomi, X. Lu, W. X. Wang, T. Aronsson, D. Shangguan, in *2006 1st Electronics Systemintegration Technology Conf.*, IEEE, Piscataway, NJ **2006**.

[53] H. Wang, A. S. Tazebay, G. Yang, H. T. Lin, W. Choi, C. Yu, *Carbon* **2016**, *106*, 152.

[54] X. Wang, P. Wu, *ACS Appl. Mater. Interfaces* **2017**, *9*, 19934.

[55] H. Jiang, Z. Wang, H. Geng, X. Song, H. Zeng, C. Zhi, *ACS Appl. Mater. Interfaces* **2017**, *9*, 10078.

[56] J. Hu, Y. Huang, X. Zeng, Q. Li, L. Ren, R. Sun, J. BinXu, C. P. Wong, *Compos. Sci. Technol.* **2018**, *160*, 127.

[57] J. W. Gu, Q. Zhang, J. Zhang, W. Wang, *Polym.-Plast. Technol. Eng.* **2010**, *49*, 1385.